

Temperature gradient analyzers for compact high-resolution X-ray spectrometers

D. Ishikawa^{a,b*} and A. Q. R. Baron^{a,b*}

Received 11 June 2009

Accepted 20 October 2009

^aMaterials Dynamics Laboratory, RIKEN/SPring-8 Center, 1-1-1 Kouto, Sayo-cho, Sayo-gun, Hyogo 679-5148, Japan, and ^bResearch and Utilization Division, JASRI/SPring-8, 1-1-1 Kouto, Sayo-cho, Sayo-gun, Hyogo 679-5198, Japan. E-mail: disikawa@spring8.or.jp, baron@spring8.or.jp

Compact high-resolution X-ray spectrometers with a one-dimensional temperature gradient at the analyzer crystal are considered. This gradient, combined with the use of a position-sensitive detector, makes it possible to relax the usual Rowland-circle condition, allowing increased space at the sample position for a given energy resolution or arm radius. Thus, for example, it is estimated that \sim meV resolution is possible with a 3 m analyzer arm and 200 mm clearance between the sample and detector. Simple analytic formulae are provided, supported by excellent agreement with ray-tracing simulations. One variation of this method also allows the detector position sensitivity to be used to determine momentum transfer, effectively improving momentum resolution without reducing (slitting down) the analyzer size. Application to medium-resolution (\sim 10–100 meV) inelastic X-ray scattering spectrometers with large angular acceptance is discussed, where this method also allows increased space at the sample. In some cases the application of a temperature gradient can improve the energy resolution even with a single-element detector.

Keywords: X-ray spectrometers; analyzer crystals; inelastic X-ray scattering; atomic dynamics; electronic dynamics.

1. Introduction

Non-resonant inelastic X-ray scattering (IXS), with a resolution of less than \sim 100 meV, is a rapidly growing field. In the high (meV) resolution limit, one has access to atomic dynamics, which are important in many phase transitions, and especially in the context of modern materials science, where the phonons are a crucial component of correlated systems. Atomic dynamics are also intimately connected with the behavior and structure of disordered materials such as liquids and glasses. Medium-resolution spectrometers, with higher intensity from relaxed resolution, can be used to measure electronic dynamics, with direct access to band structure, the multi-polarity of the electronic transitions, and to possible correlations between electronic transitions (*e.g.* dispersing excitations such as orbitons). The combination of improved instrumentation and increased access to sophisticated calculations makes measurement of the dynamic structure factor for both atoms and electrons an increasingly attractive endeavor, especially if high resolution can be obtained.

There are presently many efforts under way to improve the present generation of spectrometers, and to design the next generation of instruments, especially with new third-generation sources coming on line. In this context, the relatively

recent suggestion of ‘dispersion compensation’ by Huotari and co-workers (Huotari *et al.*, 2005), allowing improved resolution with a fixed-size spectrometer, or a smaller spectrometer for a fixed resolution, is of great interest. In principle, this is particularly true for high-resolution (\sim meV) spectrometers (Dorner & Peisl, 1983; Sette *et al.*, 1998; Burkel, 1991; Baron *et al.*, 2000; Sinn *et al.*, 2001) where the size of the 2θ (analyzer) arms can be \sim 10 m, which is very large given the limited space on the experimental floor of synchrotron radiation facilities. However, the work of Huotari *et al.* focused primarily on medium (20–100 meV) resolution, and is difficult to extend to \sim meV resolution because clearance between the sample and the detector becomes extremely restrictive. In the scheme suggested by Huotari *et al.*, this clearance, d , scales as $d = 4\varepsilon R^2/p$ where R is the arm radius, $\varepsilon = \Delta E/E$ is the fractional energy resolution, and p is the detector pixel size. Thus, for example, taking $R = 3$ m, $p = 0.1$ mm, $\Delta E = 0.3$ meV at $E = 26$ keV gives $d = 4.2$ mm, which severely limits the space for sample environment (one would really like \sim 100 mm clearance, or more).

The present paper discusses how to achieve \sim meV resolution with a short analyzer arm, while retaining a relatively large (200 mm) clearance between the detector and the sample. We show that the application of a one-dimensional

temperature gradient to the usual analyzer crystals, resulting in a corresponding gradient in the lattice spacing, allows relaxation of the Rowland-circle condition while retaining high resolution. We present a detailed analytical treatment of the various contributions supported by excellent agreement with ray-tracing simulations. While focused primarily on \sim meV energy resolution and \sim 10 mrad angular acceptance (high resolution), we also consider \sim 10 meV resolution and \sim 100 mrad acceptance (medium resolution).

The article is organized as follows. §2 reviews the basic concepts, introduces the limit of applying dispersion compensation for high-resolution work, and, qualitatively, introduces the analyzer temperature gradient. §3 presents a detailed quantitative analytic treatment of two different types of temperature gradient set-ups, and §4 discusses ray-tracing simulations and includes the effects of imperfect analyzer figure. The results for meV analyzers are discussed in §5 and application to medium resolution is covered in §6. Practical aspects, including detector size, momentum resolution and backgrounds are discussed in §7. Test results for one possible temperature gradient scheme are given in §8 and conclusions are presented in §9.

2. Basic concepts

2.1. Crystal optics

At present, sub-eV-resolution X-ray spectrometers generally use crystal analyzers; the energy resolution of most detectors remains \sim 100 eV in the hard X-ray region and, while bolometers can achieve \sim eV resolution for softer X-rays, they are far from the 0.1 eV level. Thus crystal analyzers are almost¹ the only option. Typical resolutions are given in Table 1. However, for crystal analyzers, one is severely limited by the angular acceptance of Bragg reflections in the perfect crystals, which is typically of the order of microradians, while to obtain reasonable count rates one typically desires large angular acceptance, *e.g.* 1 to 100 mrad, depending on the details of the experiment. The relation between angular acceptance and energy resolution for diffraction from a flat perfect crystal is derived from Bragg's law as

$$(\Delta E/E)_{\text{geom}} \equiv \varepsilon = \tan \delta \Delta\theta \cong \delta \Delta\theta \quad (\delta \ll 1, \Delta\theta \ll \delta), \quad (1)$$

where E is the photon energy, $\delta \simeq \pi/2 - \theta_B$ (θ_B is the Bragg angle) is a deviation angle from exact backscattering of the crystal, and ΔE is the geometric contribution to the energy

¹ In fact, nuclear resonant scattering (the Mössbauer effect) offers alternative methods of high-resolution analysis, either with the resonant isotope embedded in the sample (Seto *et al.*, 1995) or as an external analyzer foil (Chumakov *et al.*, 1996). However, the former is limited to samples containing the resonant isotope and only gives density of states information (being essentially an absorption measurement) while the latter is hampered by the mismatch of nuclear analyzer bandwidth (typically microvolts, or less) and the \sim meV monochromator bandwidth.

Table 1

Properties of the Si(*nmn*) series in an almost backscattering geometry. $\Delta E_{1\text{Flat}}$: calculated intrinsic single reflection bandwidth; $\Delta E_{2\text{Flat}}$: measured bandwidth from two flat crystals (Baron *et al.*, 2000); ΔE_{Ana} : typical observed total energy resolution with an analyzer crystal. Parentheses indicate calculated values.

n	E (keV)	$\Delta E_{1\text{Flat}}$ (meV)	$\Delta E_{2\text{Flat}}$ (meV)	ΔE_{Ana} (meV)
5	9.885	(14.5)	(21.0)	–
7	13.839	(4.8)	(6.9)	–
8	15.816	(4.1)	(5.8)	6.0
9	17.793	(1.8)	2.4	3.0
11	21.747	(0.8)	1.2	1.5
12	23.725	(0.75)	1.1	–
13	25.702	(0.35)	0.6	0.9

resolution owing to a divergence of $\Delta\theta$. Given, for example, a desired² upper limit of a geometric contribution to the resolution of 0.3 meV at 26 keV and a typical operating angle of $\delta \simeq 0.2$ mrad one finds the angular acceptance of a flat crystal is only $\Delta\theta < \sim 60$ μ rad.

To move beyond this severe limit, one usually creates a figured analyzer operating in the Rowland circle condition, where the shape of the analyzer crystal is chosen so that all rays from a point source hit it at a fixed angle, reducing or removing the geometric contribution from equation (1). For the highest resolution, one uses diced analyzers to remove strain from bending a crystal (Fig. 1A). The angular limit is then set by the crystallite size of the analyzer crystals [see discussions by Masciovecchio *et al.* (1996a,b)]. In this geometry the crystallite size in the diffraction plane, c , sets the angular scale $\Delta\theta \simeq c/L_1$ (L_1 is the sample-to-analyzer distance) giving a contribution to the energy resolution (Fig. 1A),

$$\varepsilon_1 \equiv (c/L_1) \tan \delta_0 \cong dc/2L_1^2. \quad (2)$$

The second approximation is the first-order term assuming the detector is offset a distance d from the sample. The cube size, owing to issues of fabrication, is usually ~ 1 mm. One then finds that a 0.3 meV geometric contribution at 26 keV for a 10 m arm allows $d \simeq 2.3$ mm. As L_1 (the arm radius) is reduced, this quickly becomes an even more severe limit, with d scaling as L_1^2 .

2.2. Dispersion compensation

Huotari and co-workers (Huotari *et al.*, 2005) introduced the use of a position-sensitive detector in the focal plane, essentially combining a focusing analyzer with a dispersive detector (see Fig. 1B). They showed that, assuming a sufficiently perfect analyzer figure, the block size of the crystal analyzer in (2) could be replaced by the pixel size, p , of the detector,

$$\varepsilon_2 \equiv (p/2R) \tan \delta_0 \cong dp/4R^2. \quad (3)$$

² To obtain sub-meV resolution, we consider backreflection of Si(13 13 13), which gives $\Delta E = 0.3$ meV at $E = 26$ keV.

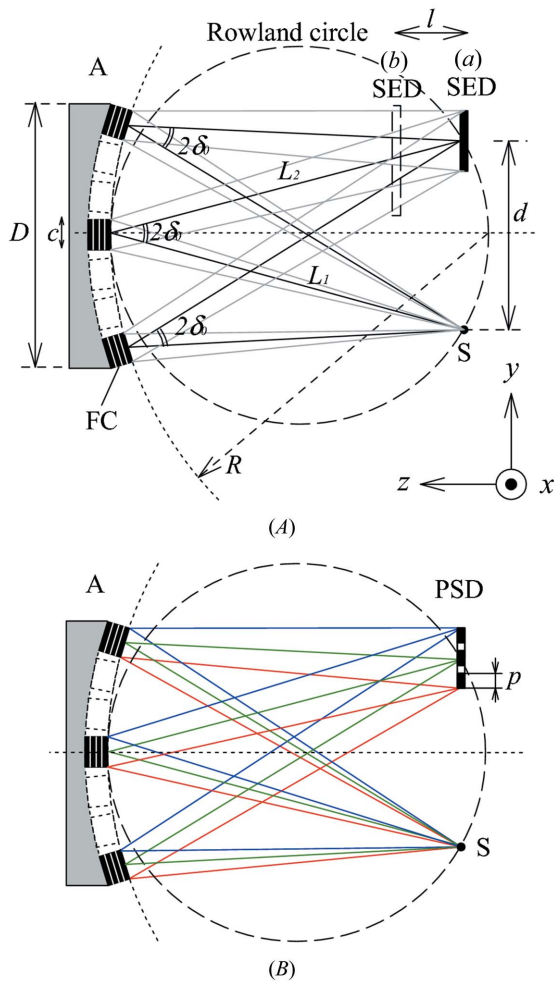


Figure 1 Schematic of conventional IXS analyzer geometries using diced crystal analyzers. (A) Rowland circle with a single detector either on the focus (solid) or offset (broken). (B) The conventional ‘dispersion compensation’ set-up with a position-sensitive detector on the Rowland circle. S: sample; A: analyzer; SED: single-element detector; PSD: position-sensitive detector; FC: flat crystallite. Parameters are listed in Table 2. The figure dimensions are exaggerated for clarity ($L_1, L_2 \gg D, l \gg d, c$).

However, this relies on strict observance of the Rowland-circle condition, with the detector directly above the sample ($L_1 = L_2 = R$). For high resolution, \sim meV, this is a very severe constraint that limits the available space at the sample to a few millimeters. For example, the detector–sample clearance, assuming a contribution of 0.3 meV at 26 keV ($\varepsilon = 1 \times 10^{-8}$) when $R = 5$ m and $p = 0.1$ mm is $d \simeq 10$ mm. This improves on the previous 2.3 mm of §2.1 but any sort of sample environment (refrigerators, furnaces, high-pressure cells) remains problematic.

2.3. Demagnification contribution and failure of dispersion compensation

One can consider focusing off the Rowland circle to make space around the sample [Fig. 2(V)]. However, this introduces variation in the Bragg angle over the analyzer surface leading to what has been called a demagnification contribution (Burkel, 1991) to the resolution given by

Table 2 Definition of parameters.

See also Figs. 1 and 2. In some cases subscripts x and y are used to indicate horizontal (out of the analyzer scattering plane) and vertical (in the analyzer scattering plane).

$\varepsilon = \Delta E/E$	Fractional energy resolution
ε_1	Geometric contribution to the resolution in a conventional configuration
ε_2	Geometric contribution to the resolution when a position-sensitive detector is used with the Rowland-circle condition satisfied; applies to both the case when the detector is in the analyzer focus (dispersion compensation) or out of the focus (with temperature gradient)
ε_3	Demagnification contribution to the resolution when the Rowland-circle condition is violated without a temperature gradient
ε_4	Contribution to the resolution when the Rowland-circle condition is violated with a temperature gradient
$\delta = \pi/2 - \theta_B$	Deviation from exact backscattering
δ_0	Deviation from backscattering at the center of the analyzer crystal
R	Radius of curvature of the analyzer crystal
L_1	Distance from sample to analyzer crystal
L_2	Distance from analyzer crystal to analyzer focal point Note: always have the thin lens equation $2/R = 1/L_1 + 1/L_2$ Note: on-Rowland is the case $R = L_1 = L_2$
d	Detector offset transverse to the beam path from center of sample to center of detector
l	Shift of the detector away from the sample toward the analyzer crystal
p	Detector pixel size transverse to beam direction in scattering plane
c	Crystallite transverse dimension
D	Size of the analyzer crystal in the scattering plane
M	Magnification L_2/L_1
δ_{\min}	Deviation on line from center of sample to lower edge of analyzer to center of detector $\delta_{\min} \simeq (1/4)\{2d/R - \Omega[(1 - M)/M]\}$
δ_{\max}	Deviation on line from center of sample to upper edge of analyzer to center of detector $\delta_{\max} \simeq (1/4)\{2d/R + \Omega[(1 - M)/M]\}$
$\Delta\delta$	Distributions of the angles onto the analyzer $\Delta\delta \equiv \delta_{\max} - \delta_{\min} = (\Omega/2)[(1 - M)/M]$ Note: upward scattering so that $\delta_{\max} \geq \delta_0 \geq \delta_{\min}$
y_a	Vertical position from center of analyzer
y_d	Vertical position from center of detector
d_{\min}	Minimum detector offset of d
T_0	Temperature at center of analyzer
T_{\min}	Minimum temperature of analyzer
T_{\max}	Maximum temperature of analyzer
ΔT	Difference of temperature from center of analyzer ($\equiv T - T_0$)
ΔE	Difference of energy of rays from elastic energy ($\equiv E - E_0$)
$2c'$	Demagnified vertical image size by off-Rowland geometry [$\equiv c(1 + M)$]

$$\varepsilon_3 \equiv \tan \delta_0 \Delta\delta \simeq \frac{d l \Omega}{4 R L_2} = \frac{d \Omega}{4 R} \frac{1 - M}{M}, \quad (4)$$

where $\Delta\delta$ is the distribution of the angles onto the analyzer defined as $\Delta\delta \equiv (\delta_{\max} - \delta_{\min})$; here δ_{\max} and δ_{\min} are maximum and minimum δ value shown [see also Figs. 2(I)(b), 2(IV), 2(V) and Table 2], and Ω is the angle of scattered rays intercepted by the analyzer, $\Omega \equiv D/L_1$, D is the analyzer size, and $M = L_2/L_1$ (see Table 2). Choosing, for example, $d = 3$ mm, $L_1 = 5$ m ($\delta_0 \simeq 0.3$ mrad), $l = 200$ mm and $\Omega = 10$ mrad, one finds a geometric contribution of $\varepsilon_3 \simeq 6.4 \times 10^{-8}$ or $\Delta E = 1.6$ meV at 26 keV. This significantly limits the achievable energy resolution.

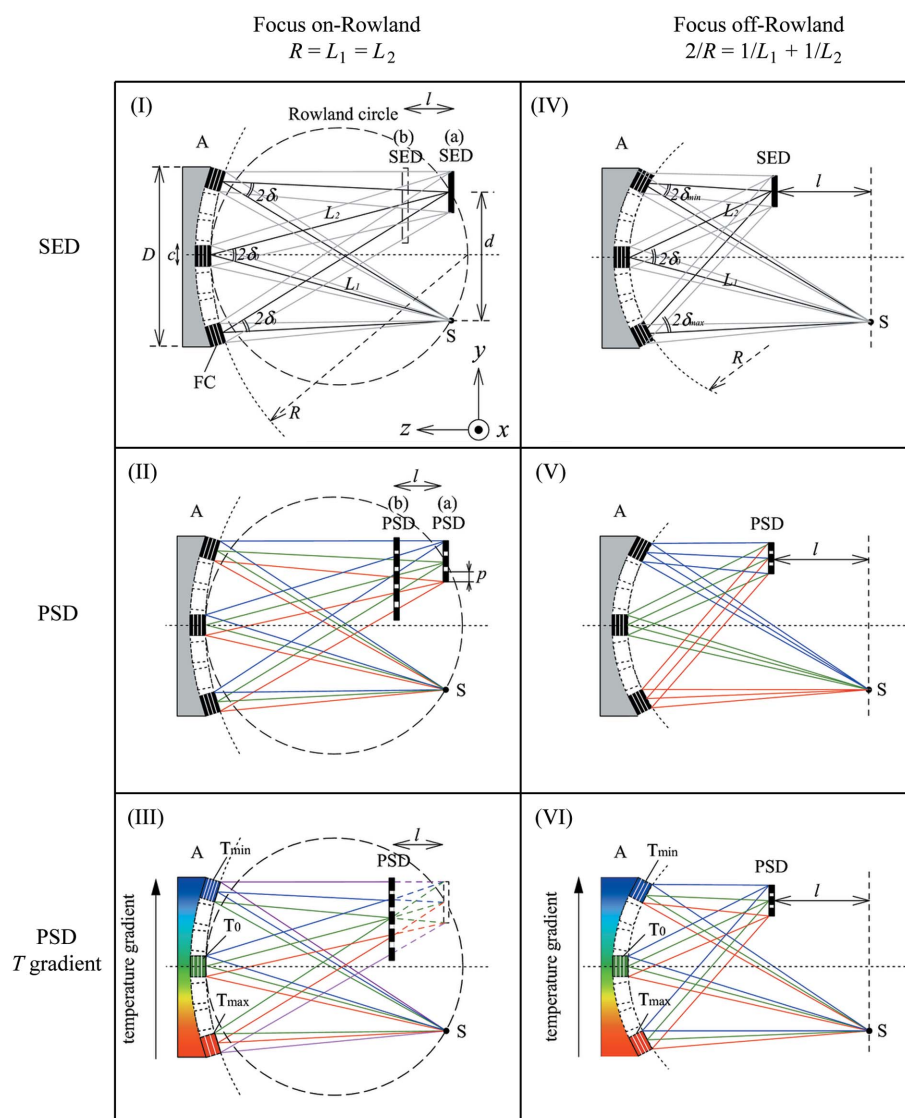


Figure 2 Schematic of IXS analyzer geometries using diced crystal analyzers. (I) Positioned along a vertical Rowland circle with single-element detector (including detector offset with focusing on-Rowland: broken square). (II) (a) Rowland geometry with a PSD, (b) focal point on the Rowland circle but detector off the circle. (III) Focusing on-Rowland but detector in front of focal point. (IV) Focusing off-Rowland with a single-element detector, demagnification contribution causes chromatic aberration. (V) Detector offset with PSD; energy–position correspondence in (II) is broken in (V). (VI) Temperature gradient of the analyzer crystal ($T_{\min} < T_0 < T_{\max}$); temperature correction reduces chromatic aberration and allows off-Rowland geometry to be used. Colored lines indicate dispersed energy for clarity, e.g. the different color of the rays are focused on the center of the detector in case (V), while one color of the rays are focused on the same position in case (VI).

2.4. Temperature gradient analyzers: qualitative

To a first approximation, the temperature gradient we suggest here may be considered as a way of modifying the lattice constant to compensate for the demagnification contribution, essentially varying the d -spacing to correct for the variation in the Bragg angle, δ , over the analyzer. This allows us to introduce the idea, and sets the scale for the required gradient, though a different, and, in some cases, better, method will also be described below. The magnitude of the required temperature gradient over the analyzer is roughly

attractive.

Before proceeding, we introduce another important parameter, the clearance between the divergent beam scattered from the sample to the analyzer and the beam reflected from the analyzer into the detector. The minimum clearance, so that the detector does not occlude the analyzers and so that the entire reflected beam is collected by the analyzer, is denoted d_{\min} . Note that choosing $d = d_{\min}$ leaves no space for either a border around the detector or for shielding. By default, we will take $d = d_{\min} + 2$ mm to allow for these.

given as $\Delta T = \varepsilon_3/\alpha$ where α is the thermal expansion coefficient of the analyzer and ε_3 is the demagnification contribution from equation (4). Taking the previous case ($d = 3$ mm, $L_1 = 5$ m, $l = 200$ mm and $\Omega = 10$ mrad), one can estimate the required gradient to be about 25 mK over a silicon analyzer operated at room temperature ($\alpha = 2.6 \times 10^{-6} \text{ K}^{-1}$). This is a small, but crucial, adjustment to achieving high resolution. It becomes more important as the arm radius is further reduced.

3. Temperature gradient analyzers: quantitative

Detailed discussion of the temperature gradient depends on the precise focusing conditions. In the preceding section, the temperature gradient was introduced as a response to the demagnification contribution when one moved the analyzer focus off the Rowland circle. However, there are actually two limiting cases: one where the analyzer focus remains on the Rowland circle and only the detector is moved away from the sample, and one where both the analyzer focus and the detector are moved off the Rowland circle together. These will be referred to as the ‘on-Rowland’ and ‘off-Rowland’ cases, respectively, where the designation refers to the position of the analyzer focus. These are shown in Fig. 2, where cases (I)–(III) are all on-Rowland while (IV)–(VI) are off-Rowland. The temperature gradient can be used to improve the resolution in both cases. Considering resolution only, the on-Rowland case is better. However, practical considerations (beam size and detector noise) can make the off-Rowland geometry

3.1. Temperature gradient for focus on-Rowland [case (III)]

Here we discuss the situation described by Fig. 2(III). The analyzer focus remains on the Rowland circle, so very near to the sample, but the detector is moved towards the analyzer to make space at the sample position. Applying a proper temperature gradient allows preservation of a (nearly) unique energy–position correlation in the detector despite the detector being out of the analyzer focus. Considering Fig. 3, the temperature gradient preserves the linear relationship between energy and position [shown in Fig. 3(II)(a)], but increases its range [Fig. 3(III)].

The exact form of the correlation between temperature and position on the analyzer is derived as follows. For a fixed angle of incidence the energy difference between rays reflected by two different crystal cubes having temperature T and T_0 is $\Delta E/E = d_{hkl}(T_0)/d_{hkl}(T) - 1$, where $d_{hkl}(T)$ is the d -spacing at temperature T . Meanwhile, neglecting the cube size of the analyzer ($c \rightarrow 0$) and using equation (3), the energy offset and detector vertical displacement, y_d , are related by $\Delta E/E = (y_d/2R') \tan \delta_0$. Here, R' satisfies $2/R' = 1/L_1 + 1/(L_1 - l)$ and y_d can be replaced by the analyzer y -position (y_a) in Fig. 2(VI) using $y_d \simeq ly_a/L_1$. Then the relation between y_a and temperature deviation $\Delta T (\equiv T - T_0)$ is

$$y_a(\Delta T) \simeq \left[\frac{d_{hkl}(T_0)}{d_{hkl}(T)} - 1 \right] \frac{2R'L_1}{l \tan \delta_0} \simeq -\frac{4R'^2 L_1}{ld} \alpha(T_0) \Delta T, \quad (5)$$

where

$$d_{hkl}(T) = d_{\text{ref}} \left[1 + \int_{T_{\text{ref}}}^T \alpha(T') dT' \right] \simeq d_{\text{ref}} [1 + \alpha(T_0) \Delta T],$$

and the second equality assumes the thermal expansion coefficient, $\alpha(T)$, is approximately temperature independent. Precise values of $\alpha(T)$ for silicon may be found by Watanabe *et al.* (2004) and Okada & Tokumaru (1984), and a reference lattice constant $a_{\text{ref}} = 5.43102 \text{ \AA}$ at $T_{\text{ref}} = 295.65 \text{ K}$ (Mohr & Taylor, 2000). Taking the center of the analyzer to be at temperature $T_0 = 300.000 \text{ K}$, we may write $d_{hkl}(T_0)/$

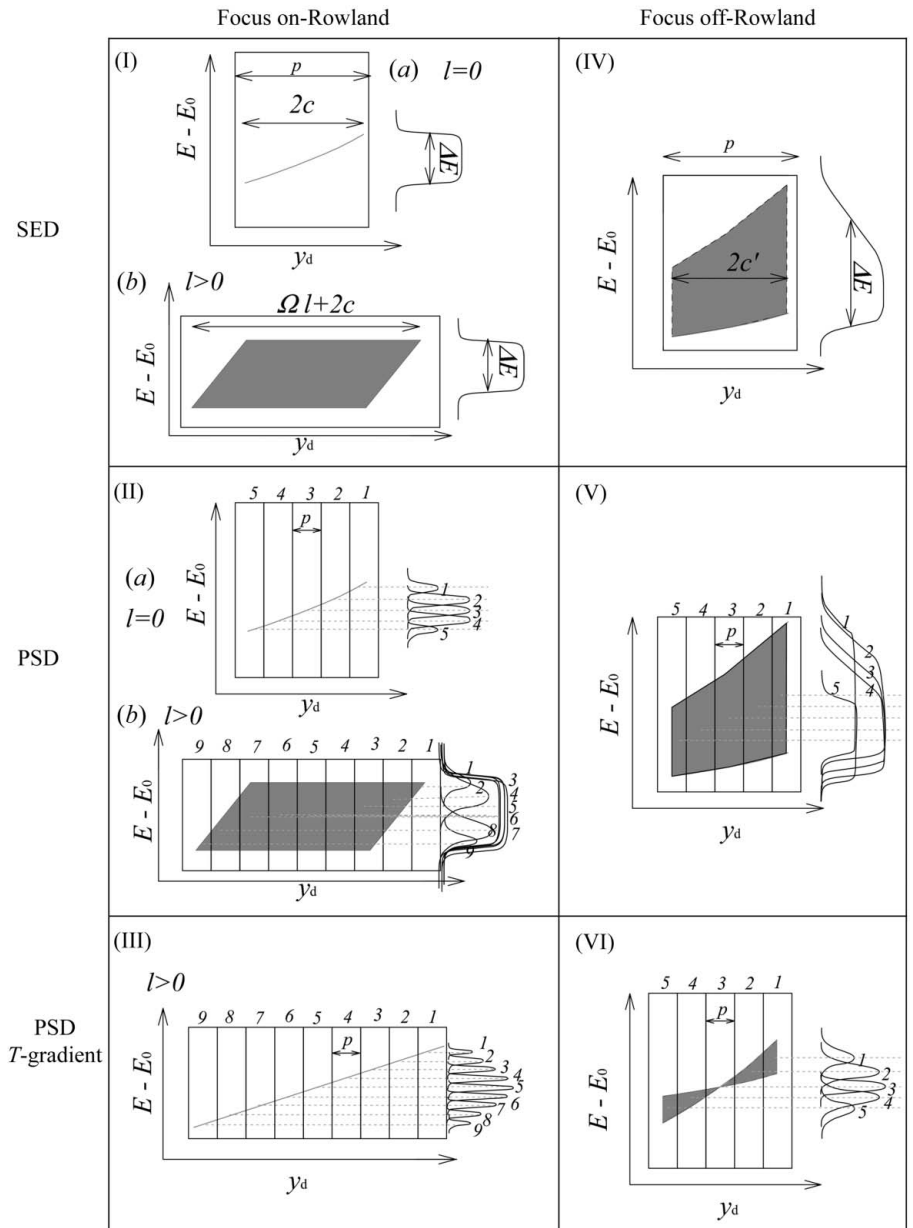


Figure 3

Schematic of the energy–position correlation in the six different geometries of Fig. 2. Right-hand line shapes are projections of the resolution function of each detector element. $E - E_0$: relative energy, y_d : detector y -position; p : detector pixel size; $2c$: image size of the small cube crystal. $2c'$: demagnified image size. The temperature gradient of the analyzer reduces the aberration [(III), (VI)].

$$d_{hkl}(T) - 1 \simeq -\alpha(T_0) \simeq -2.627879 \times 10^{-9} \Delta T [\text{mK}] + O(\Delta T)^2.$$

Fig. 4(a) shows the required temperature gradient as a function of normalized analyzer dimension for $L_1 = 3, 6, 10 \text{ m}$, $l = 200 \text{ mm}$ and, as mentioned above, $d = d_{\text{min}} + 2 \text{ mm}$. In this geometry, assuming perfect analyzer figure and a point source, d_{min} is given by

$$d_{\text{min}} = \Omega l + c \quad (\text{focus on-Rowland}), \quad (6)$$

where Ωl is the vertical size of the beam to the analyzer at a distance l from the sample. The temperature gradient is linear

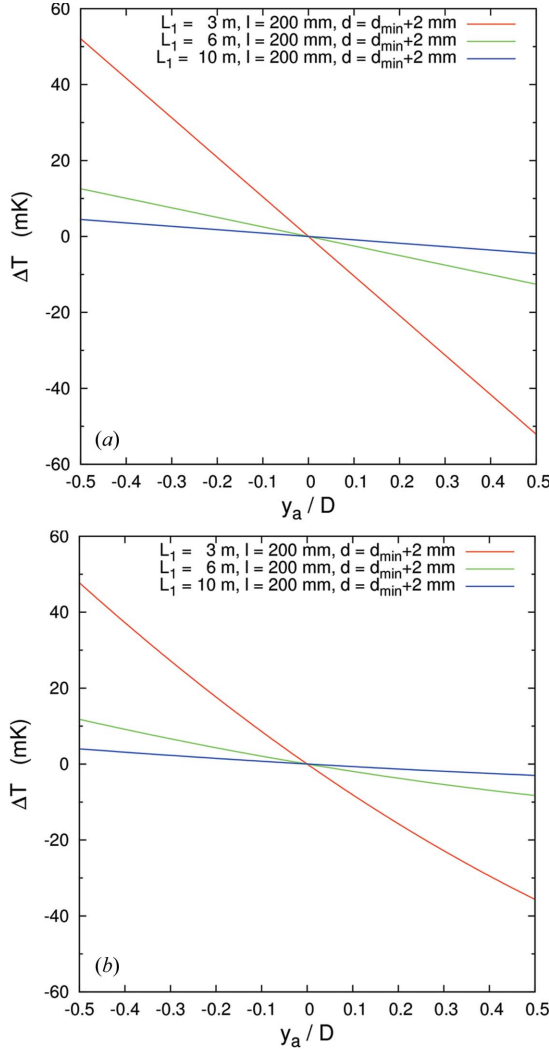


Figure 4
Temperature gradient curve ΔT as a function of analyzer y -position (y_a) normalized by the analyzer dimension. Optical geometry is (a) focus on-Rowland [case (III)] and (b) focus off-Rowland [case (VI)]. Each geometry compares $L_1 = 3.0, 6.0$ and 10.0 m and $D = 30, 60, 100$ mm. Note the more nearly linear behavior in (a).

and the ranges are $\pm 52, \pm 12.6$ and ± 4.5 mK relative to the center of the analyzer, respectively.

3.2. Temperature gradient for focus off-Rowland [case (VI)]

Here we discuss the situation described by case (VI) of Figs. 2 and 3. The analyzer focus remains in the detector as it is moved off the Rowland circle, introducing a demagnification contribution, which is then compensated by the temperature gradient. Considering Fig. 3, one can consider the gradient as a way of collapsing the dispersion over the detector [Fig. 3(V)] to a more almost linear form [Fig. 3(VI)]. This is essentially a first-order correction to the demagnification contribution. However, owing to the range of Bragg angles now going to the analyzer focal point, the slope of the energy dispersion *versus* detector position depends on the position in the analyzer where the reflection occurs, thus the correction is only perfect for one position in the detector. However, it still reduces the

measured bandwidth. This may be analyzed in detail as follows. For an off-circle focus the analyzer radius, R , is given by the usual lens equation³

$$\frac{2}{R} = \frac{1}{L_1} + \frac{1}{L_2} \quad (7)$$

where, as shown in Fig. 2(IV) and Table 2, L_1 is the distance from the sample to the analyzer, and L_2 is that from the analyzer to the focal point. The detector is at $l = L_1 - L_2$. The required condition to keep the energy constant over the analyzer then becomes $d_{hkl}(T) \cos \delta = \text{constant}$. Taking T_0 and δ_0 as the temperature and angle at the center of the analyzer, $y_a(\Delta T)$ is expressed as

$$\begin{aligned} y_a(\Delta T) &\simeq 2 \left\{ \frac{d}{2R} - \cos^{-1} \left[\cos \delta_0 \frac{d_{hkl}(T_0)}{d_{hkl}(T)} \right] \right\} / \left(\frac{1}{L_2} - \frac{1}{L_1} \right) \\ &\simeq \frac{2 \left\{ \delta_0 - [2\alpha(T_0)\Delta T + \delta_0^2]^{1/2} \right\}}{(1-M)/(L_1 M)}. \end{aligned} \quad (8)$$

This may be inverted to give

$$\Delta T(y_a) \simeq \frac{1}{8\alpha(T_0)} \left(\frac{1-M}{L_1 M} \right) \left[-4\delta_0 + \left(\frac{1-M}{L_1 M} \right) y_a \right] y_a. \quad (9)$$

Note that, in contrast to §3.1, the second-order term is no longer negligible. Then the minimum detector offset in this geometry is given as

$$d_{\min} = \frac{\Omega l}{2} + c' \quad (\text{focus off-Rowland}), \quad (10)$$

where the image from a single block of the analyzer will have a size reduced by the shorter path length to the detector, $2c' = c(1+M)$.

Fig. 4(b) shows the temperature gradient ΔT as a function of normalized analyzer dimension for parameters $L_1 = 3, 6$ and 10 m and $l = 200$ mm and $d = d_{\min} + 2$ mm. The temperature gradient is not linear, and ranges from $+48$ to $-35, +11$ to -9 and $+4$ to -3 mK, respectively. The energy–position correlation becomes quadratic as seen in Fig. 3(VI). The energy–position density is also not uniform and may yield asymmetric line shapes for the resolution function.

If the temperature gradient given by (8) is applied, then the full width of the energy distribution at the edge of the detector [seen in Fig. 5(d) or Fig. 9(d)] is $\varepsilon = (c'/2R)\Delta\delta$. Assuming the detector pixel size is relatively small compared with the beam size, this contribution is reduced when the integration (with appropriate energy shift) over the detector is performed. In addition, we note that the quadratic dependence of the energy shift on the position in the analyzer leads to a concentration of the intensity near the central (small slope) line in these figures. Thus the practical contribution to the energy shift in this case is about $(c'/2R)\Delta\delta/4$. This is, perhaps, more easily seen in Figs. 5(c) and 9(c), which, after applying the temperature gradient, are essentially compressed into Figs. 5(d) and 9(d), but the weighting remains very asymmetric. The pixel size

³ Strictly speaking, $2/(R \cos \delta_0) = 1/L_1 + 1/L_2$ is the best focusing condition. However, in this paper, δ_0 is small so that one can omit the $\cos \delta_0$ term: δ_0 is 10 mrad then $1 - \cos \delta_0$ is only 5×10^{-5} .

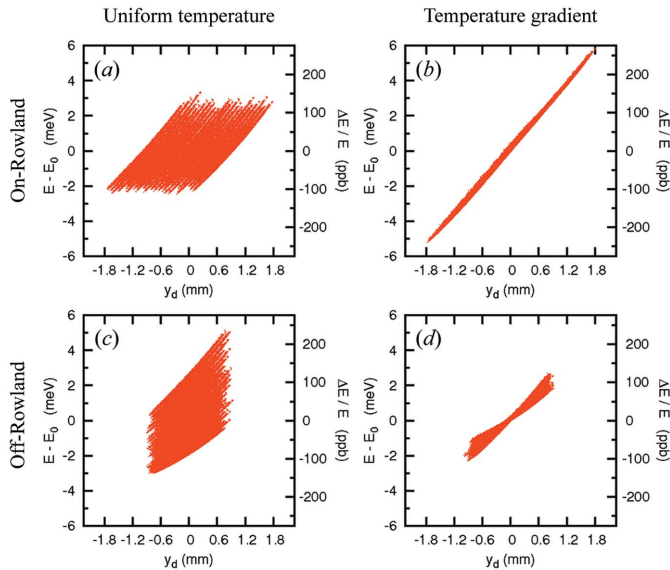


Figure 5 Energy–position correlation in the detector. (a) and (b) are for the on-Rowland case without or with temperature gradient of the analyzer crystal; (c) and (d) are for the off-Rowland geometry without or with temperature gradient. $E = 21.747$ keV for Si(11 11 11) backreflection case from the ray-tracing results. Optical geometry: $L_1 = 3$ m, $l = 200$ mm and (a) $d = 4.60$ mm and (b) $d = 3.56$ mm are considered here. Contributions from analyzer slope error, $\sigma_{(x,y)} = 20 \mu\text{rad} \times 20 \mu\text{rad}$, and source size $\sigma_{\text{ss}(x,y)} = 20 \mu\text{m} \times 20 \mu\text{m}$, are included.

contribution is most accurately represented by using δ_{max} in (3). The energy resolution in this case is then given by

$$\begin{aligned} \varepsilon_4 &\equiv \frac{p}{2R} \tan \delta_{\text{min}} + \frac{1}{4} \frac{c'}{2R} \Delta\delta \\ &\simeq \frac{1}{8R} \left[\Omega \frac{1-M}{M} \left(\frac{c'}{2} - p \right) + \frac{2pd}{R} \right]. \end{aligned} \quad (11)$$

It is worth noting that the non-linear energy–position correlation of this geometry owing to the variation in δ over the analyzer surface leads to a slightly worse energy resolution. Also a non-linear temperature gradient may be difficult to achieve practically. However, in contrast to the focus on-Rowland case, the image size at the detector is reduced, as shown in Table 3. Therefore detector size can be smaller, reducing d_{min} and the detector background (see §7).

It is also worth noting that spherical aberration originates from the deviation from ideal aspherical shape (ellipsoidal) causing blurring of the focusing beam size, $\Delta s_{\text{ellip-spher}}$, and may degrade energy resolution. However, this is only problematic when the solid angle is much larger and magnification is much smaller. This contribution is negligible as far as geometries in this article are considered.⁴

As a final comment, we note that the off-Rowland case may also be applied without the detector in the analyzer focus. This may be advantageous in some cases.

⁴ The maximum spherical aberration is $(D^3/16R^2)[(1 - M^2)/M^2]$. One can calculate a worst-case blurring of $\sim 16 \mu\text{m}$ for $L_1 = 1$ m, $l = 0.1$ m and $\Omega = 100$ mrad.

Table 3

Properties of two focusing geometries: focus on-Rowland circle [case (III)] and focus off-Rowland circle [case (VI)].

Notation of the optical parameters are explained in the text.

	Focus on-Rowland	Focus off-Rowland
Sample–detector minimum vertical offset, d_{min}	$\Omega l + c$ (larger)	$\Omega l/2 + c'$ (smaller)
Image size (detector active area, y -direction)	$\Omega l + 2c$ (larger)	$2c'$ (smaller)
Energy–position correlation	Linear	Quadratic
Temperature gradient	Linear	Quadratic
Energy resolution	$\varepsilon_2 = (p/2R) \tan \delta_0$	$\varepsilon_4 = (p/2R) \tan \delta_{\text{min}} + (c'/8R) \Delta\delta$

4. Ray-tracing

Ray-tracing simulations were performed to confirm the accuracy of the analytic formulae of the previous section. Analyzer crystals were taken to be rectangular with dimensions D_x and D_y , and to have either a spheroidal or toroidal curvature. (Note that x and y refer to the two directions perpendicular to the reference X-ray path, z , perpendicular and within the scattering plane.) Also, note that while we carefully considered finite extent transverse to the analyzer scattering plane, it had negligible impact in all cases considered. Analyzers are assumed to be ‘diced’ with, for example, crystallite sizes of $0.6 \text{ mm} \times 0.6 \text{ mm}$ on a 0.7 mm pitch. The simulations, using geometrical optics, generally traced more than 200000 rays with those rays spread over more than 400 analyzer crystallites, with >400 rays per crystallite. The selected crystallites were uniformly distributed on the analyzer surface in both x and y directions transverse to the sample–analyzer axis, as were the rays on each crystallite. Each selected crystallite was assumed to have a deviation in orientation from the ideal (spheroidal or toroidal) surface given by a Gaussian distribution to simulate errors in manufacture. The source point (*i.e.* over the sample) for a given ray was also randomly selected for each ray within a Gaussian distribution of size $\sigma_{\text{ss},x}, \sigma_{\text{ss},y}$ to simulate the finite beam size on the sample (or finite penetration into the sample). This allows definition of the exact incident angle of each ray onto a crystallite, and, with specular reflection assumed⁵, then defines the point of intersection in the detector.

Aside from the geometric parameters defining the set-up, the reflection curve (in the form of reflected intensity *versus* energy for a fixed and perfectly defined angle near to back-scattering) is also required as an input parameter. The transformation from angular deviation to energy shifts was made using Bragg’s law (without linearization). This input reflectivity curve was usually chosen to agree with that calculated from dynamical diffraction from a thick crystal using the Si(nmn) series of reflections as listed in Table 1. However,

⁵ Effects from the finite penetration into the analyzer crystal (which can be estimated to spread a well defined beam, over a length $\sim 2\delta_0 \lambda_{\text{abs}}$) were neglected. This contribution is much smaller than cube size or detector pixel size so that one can assume reflection occurs specularly at the surface of the flat cube.

when only the geometric contribution to the energy was desired, then a narrow delta-function-like reflectivity curve (width <0.05 meV) was used. After setting the geometry and choosing the input reflectivity curve, the incident energy was scanned assuming that the analyzer temperature was held stable. The resulting distributions are then integrated over individual detector pixels, giving curves of intensity as a function of incident energy for a given detector pixel. This is then convolved with an incident energy distribution appropriate for the monochromator defining the bandwidth onto the sample.

5. Parameters, results and discussion for meV resolution

The parameter space is complex, with many free parameters relating to the desired performance and size of the spectrometer. In this section we focus on parameter sets aimed at achieving high, \sim meV, resolution, with an accepted solid angle in the analyzer of 10 mrad, consistent with taking $\Delta Q \simeq 1 \text{ nm}^{-1}$. In the next section, §6, we consider medium resolution.

5.1. Analyzer and source parameters

Experience in fabrication of analyzer crystals with large, 9.8 m, radii of curvature (Miwa, 2002) leads us to take $\sigma_{x,y} = 20 \mu\text{rad}$ as the r.m.s. deviation of the analyzer crystallites in each direction. It is possible that this may increase for smaller radii of curvature, but the effect of such deviation, generally scaling as $R\sigma$, will be reduced by the smaller radius. The source size, or the illuminated volume of the sample projected normal to the sample-analyzer direction, was chosen to be $\sigma_{ss(x,y)} = 20 \mu\text{m}$ (47 μm FWHM), consistent with a focused beam at a typical spectrometer. The solid angle of the analyzer crystal in the vertical was fixed at 10 mrad. This is broadly consistent with present spectrometer design.

5.2. Spectrometer and detector parameters

The space between the sample and the detector, l , was set at 200 mm, as being comparable with present-day spectrometers with longer 2θ arms. The clearance between the active edge of the detector and the beam was taken as 2 mm, or $d = d_{\text{min}} + 2$ mm, as discussed above. The detector pixel size was set at $p = 0.3$ mm. In principle, this might be reduced 0.17 or 0.05 mm, consistent with pixel sizes of various detectors. However, the 0.3 mm value is comparable with the effect of blurring owing to analyzer deviation due to the 20 μrad angular variation. It is also consistent with the thickness of typical silicon pixel detectors, which can be the relevant parameter if such a detector is used at grazing incidence to improve the stopping power. In general, while it is easy to consider reducing the pixel size below 0.3 mm, it must be done with care as, to see some benefit from this, many things must be improved simultaneously. The 0.3 mm chosen here is comfortably matched to the present conditions. The (one-dimensional)

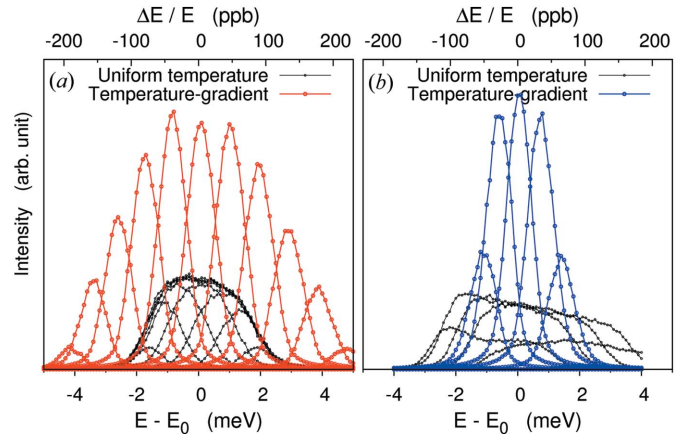


Figure 6

Resolution functions of PSD scanning, incident photon energy 0.1 meV step relative to elastic line. $E = 21.747$ keV for the Si(11 11 11) backreflection case. (a) Focus on-Rowland. (b) Focus off-Rowland. For comparison, the uniform temperature case of the analyzer is shown. Optical geometry of $L_1 = 3$ m, $l = 200$ mm, $d = 4.60$ mm (a) and $d = 3.56$ mm (b) are considered here. Angular deviation from ideal surface $\sigma_{(x,y)} = 20 \mu\text{rad} \times 20 \mu\text{rad}$, source size $\sigma_{ss(x,y)} = 20 \mu\text{m} \times 20 \mu\text{m}$ and intrinsic Darwin width $\Delta E_{\text{int}} = 0.8$ meV are taken into account. (Incident bandwidth is eliminated.)

temperature gradient of the analyzer crystal is assumed to be given by equation (5) or equation (9).

5.3. Representative results: energy–position correlation and energy resolution

As an example, we discuss the parameter set for $L_1 = 3$ m, listed in Table 4 [(III) and (VI)]. The spheroid surface of Rowland circle diameter $R_x = 3000$ mm (horizontally) and $R_y = 3000$ mm (vertically) was taken for case (III). Meanwhile, for case (VI), a toroidal surface of diameter $R_x = 3000$ mm and $R_y = 2897$ mm⁶ was taken. The energy–position correlation in the detector in this selected geometry is shown in Fig. 5(a) for the on-Rowland geometry. The chromatic aberration owing to the demagnification contribution in Fig. 5(a) is reduced by use of the temperature gradient in Fig. 5(b), even though fabrication imperfections have been included in §5.1. As shown in Fig. 5(d), the temperature gradient also drastically reduces the aberration from Fig. 5(c).

Fig. 6 shows resolution functions from pixels calculated by scanning the incident photon energy across the elastic energy. The FWHM of the spectra of individual pixels gives $E_{\text{tot}}^{\text{sim}} = 1.12$ meV⁷ (on-Rowland) and 1.0 meV⁸ (off-Rowland) at Si(11 11 11) assuming a delta-function incident bandwidth. As shown in Fig. 6(a), these agree well with the analytical estimation $E_{\text{tot}}^{\text{ana}} = 1.15$ and 1.0 meV (FWHM), respectively. To provide a comparison with a uniform temperature [$T(y_a) =$

⁶ The horizontal radius of curvature R_x affects the horizontal size of the focused beam but does not affect the energy resolution or the temperature gradient for cases considered in this paper. See also §7.

⁷ The geometric term of the resolution is calculated as $\Delta E_{\text{geom}}^{\text{sim}} = 0.97$ meV (FWHM)

⁸ $\Delta E_{\text{geom}}^{\text{sim}} = 0.59\text{--}0.71$ meV (FWHM) depending on the position of the detector pixels.

Table 4

Calculated contributions to energy resolution in (I)–(VI).

Parameters are defined in Table 2. Analyzer crystal dimension $D = 100, 60$ and 30 mm is chosen to keep the solid angle $\Omega = 10$ mrad. ΔT_1 and ΔT_2 are top and bottom temperature offset relative to the analyzer center. ε_1 to ε_4 are contributions to the energy resolution discussed in the text. $(\Delta E)_{\text{geom}}$: geometric energy resolution at $E = 21.747$ keV. $(\Delta E)_{\text{sim}}$: ray-tracing results, only geometric contributions are taken into account. Si(13 13 13) backreflection case at $E = 25.702$ keV are also shown in $(\Delta E)_{\text{geom}}$.

	(I)(a)			(II)(a)			(III)			(IV)			(V)			(VI)		
L_1 (m)	10	6	3	10	6	3	10	6	3	10	6	3	10	6	3	10	6	3
L_2 (m)	10	6	3	10	6	3	10	6	3	9.8	5.8	2.8	9.8	5.8	2.8	9.8	5.8	2.8
R (m)	10.00	6.000	3.000	10.00	6.000	3.000	10.00	6.000	3.000	9.899	5.898	2.897	9.899	5.898	2.897	9.899	5.898	2.897
c (mm)	0.6	0.6	0.6	0.6	0.6	0.6	0.6	0.6	0.6	0.6	0.6	0.6	0.6	0.6	0.6	0.6	0.6	0.6
d (mm)	2.60	2.60	2.60	2.60	2.60	2.60	4.60	4.60	4.60	3.59	3.59	3.58	3.59	3.59	3.58	3.59	3.59	3.58
l (mm)	0.0	0.0	0.0	0.0	0.0	0.0	200	200	200	200	200	200	200	200	200	200	200	200
p (mm)	–	–	–	0.3	0.3	0.3	0.3	0.3	0.3	–	–	–	0.3	0.3	0.3	0.3	0.3	0.3
M	1.00	1.00	1.00	1.00	1.00	1.00	1.00	1.00	1.00	0.98	0.97	0.93	0.98	0.97	0.93	0.98	0.97	0.93
δ_0 (mrad)	0.13	0.22	0.43	0.13	0.22	0.43	0.23	0.39	0.79	0.18	0.30	0.62	0.18	0.30	0.62	0.18	0.30	0.62
$\Delta\delta$ (mrad)	0.0	0.0	0.0	0.0	0.0	0.0	0.0	0.0	0.0	0.10	0.17	0.36	0.10	0.17	0.36	0.10	0.17	0.36
ΔT_1 (mK)	0	0	0	0	0	0	–4.5	–12.6	–52.1	0	0	0	0	0	0	0	0	0
ΔT_2 (mK)	0	0	0	0	0	0	4.5	12.6	52.1	0	0	0	0	0	0	0	0	0
ε_1 (p.p.b.)	8	22	87	–	–	–	–	–	–	–	–	–	–	–	–	–	–	–
ε_2 (p.p.b.)	–	–	–	2	5	22	3	10	40	–	–	–	–	–	–	–	–	–
ε_3 (p.p.b.)	–	–	–	–	–	–	–	–	–	19	52	221	19	52	221	–	–	–
ε_4 (p.p.b.)	–	–	–	–	–	–	–	–	–	–	–	–	–	–	–	3	8	32
ε (p.p.b.)	8	22	87	2	5	22	3	10	40	19	52	221	19	52	221	3	8	32
$(\Delta E)_{\text{geom}}$ (meV)†	0.17	0.47	1.88	0.04	0.12	0.47	0.08	0.21	0.86	0.40	1.14	4.80	0.40	1.14	4.80	0.06	0.17	0.69
$(\Delta E)_{\text{sim}}$ (meV)	0.16	0.46	1.86	0.06 (±0.002)	0.12 (±0.01)	0.47 (±0.06)	0.08	0.21	0.97	0.38	1.06	4.27	0.40 (±0.03)	1.11 (±0.10)	4.4 (±0.4)	0.068– 0.078	0.15– 0.18	0.59– 0.71
$(\Delta E)_{\text{geom}}$ (meV)‡	0.20	0.56	2.23	0.05	0.14	0.56	0.09	0.25	1.02	0.48	1.34	5.64	0.48	1.34	5.64	0.07	0.20	0.81

† $E = 21.747$ keV. ‡ $E = 25.702$ keV.

constant], ray-tracing results are also shown for this case in Fig. 6 (black symbols). In this geometry the energy resolution decreases by a factor of three (on-Rowland) to six (off-Rowland) when the temperature gradient is applied.

5.4. Discussion

Here, we consider the dependence of the energy resolution on the spectrometer size, L_1 . Using analytic forms discussed in §2, the energy resolution as a function of 2θ arm length L_1 is summarized in Fig. 7, expressed by solid (geometric contribution) and broken (total contribution) lines.⁹ Table 4 lists the results of Fig. 7. Ray-tracing results, using parameters in Table 4, are shown by circles. This shows that it is possible to estimate resolution using the analytic approximations with a fair degree of accuracy. The effect of the temperature gradient becomes large beginning near 6 m. An energy resolution of ~ 1.5 meV is possible at 21.7 keV for $L_1 > 3$ m.

6. Medium-resolution with large angular acceptance

We now consider application to medium-resolution large-solid-angle analyzers. This is the case originally considered for dispersion compensation without a temperature gradient (Huotari *et al.*, 2005, 2006). While more space is available near the sample in this case since the resolution is relaxed, it is still limited, so it is attractive to consider moving the detector away

⁹ $\varepsilon_{\text{tot}} \equiv (\varepsilon_{\text{geom}}^2 + \varepsilon_{\text{slope}}^2 + \varepsilon_{\text{source}}^2 + \varepsilon_{\text{int}}^2)^{1/2}$. Here, $\varepsilon_{\text{slope}}$ and $\varepsilon_{\text{source}}$ are given by $2.35\sigma \tan \delta_0$ and $2.35\sigma_{\text{ss}} \tan \delta_0$, respectively. ε_{int} is the intrinsic reflection width of a specified diffraction plane.

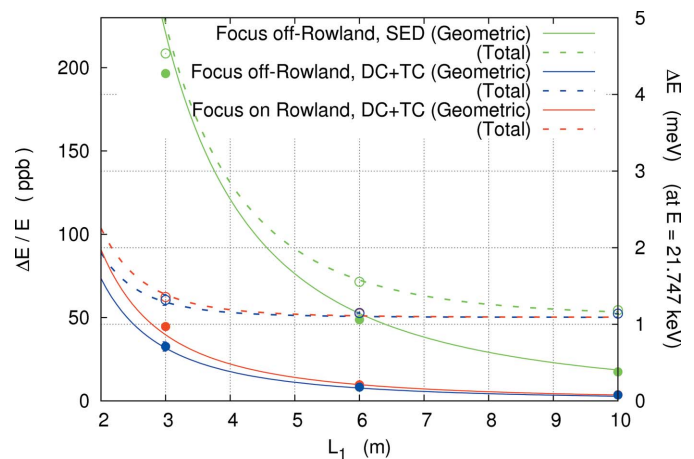


Figure 7

Energy resolution as a function of 2θ arm length L_1 for high-resolution spectrometers. Comparison of a single-element detector (SED) and dispersion compensation (DC) with temperature compensation (TC). Closed and open circles represent simulation results of geometric and total contributions, respectively. Solid lines are the geometric terms discussed in Table 4. Broken lines are the estimated total resolution including non-perfection contributions.

from the sample. In contrast to high-resolution IXS, medium-resolution set-ups often employ large-solid-angle analyzers ($\Omega = 50$ – 100 mrad) to increase count rate. In this case, while the formulae given in §3 remain applicable as a first approximation, some care is needed and ray-tracing becomes increasingly important. Here we focus on shorter (1–2 m-long) arms and a fixed large analyzer crystal $D_{(x,y)} = 100$ mm. We

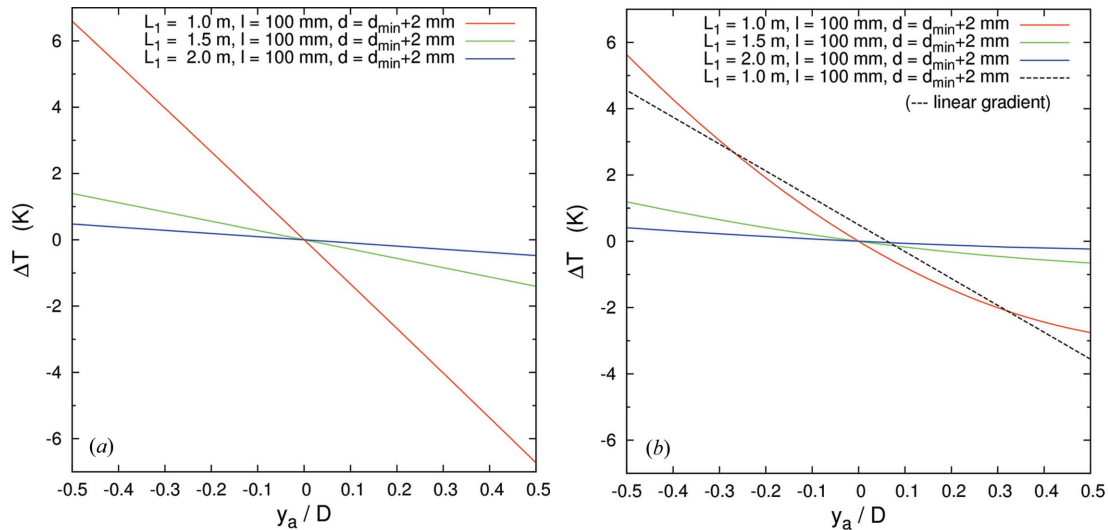


Figure 8 Temperature gradient for medium resolution for (a) focus on-Rowland [case (III)] and (b) focus off-Rowland [case (VI)]. The temperature deviation ΔT as a function of analyzer y -position (y_a) normalized by analyzer dimension $D = 100$ mm is shown for silicon analyzers with central temperature 300 K.

consider the Si(555) reflection at $E = 9.9$ keV which has an intrinsic resolution (single reflection) of 14.6 meV. We take $l = 100$ mm.

In contrast to the high-resolution analyzers, the temperature gradient of the present case (smaller arm and large solid angle) becomes much steeper as seen in Fig. 8. The corresponding energy–position characteristics are shown in Fig. 9. Another important point is that the magnitude of the image at the detector increases quickly with increasing Ωl . When $\Omega = 100$ mrad, $l = 100$ mm, one can estimate the image size to be

11.2 mm. This is much larger than one-to-one focusing (on-Rowland geometry) image size ($2c = 1.2$ mm) and requires a large number of detector pixels (see Fig. 10a), and may make the off-Rowland geometry relatively attractive.

The energy resolution as a function of L_1 is shown in Fig. 11. One can obtain a resolution almost the same as the intrinsic reflection width $\Delta E \simeq 15$ meV listed in Table 1. This drastically increases when $L_1 < \sim 1$ m. For $\Delta E < 20$ meV, one requires $L_1 > \sim 1$ m.

Before closing this section, it is worth noting that the application of a temperature gradient can improve the energy resolution even when a single-element detector is used. This works in the off-Rowland geometry [case (VI) in Fig. 2]. Fig. 12 shows results for $L_1 = 1$ m, $\Omega = 100$ mrad, $l = 100$ mm. Ray-

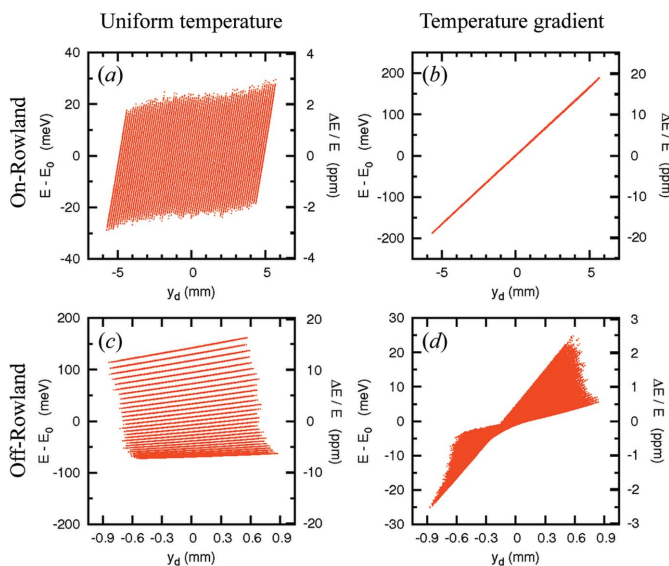


Figure 9 Energy–position correlation in the detector by ray-tracing. $E = 9.885$ keV, Si(555) backreflection case. y_d : detector vertical position. $E - E_0$: relative energy. Optical geometry of $L_1 = 1$ m, $l = 100$ mm and (a) $d = 12.60$ mm and (b) $d = 7.54$ mm are considered here. Contributions from slope error $\sigma_{(x,y)} = 20 \mu\text{rad} \times 20 \mu\text{rad}$, source size $\sigma_{ss(x,y)} = 20 \mu\text{m} \times 20 \mu\text{m}$ are included

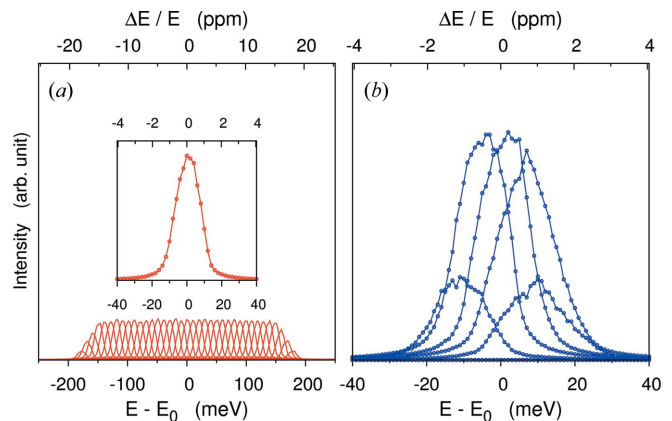


Figure 10 Resolution functions: (a) focus on-Rowland (b) focus off-Rowland. The inset in (a) is magnification of results for one pixel. $E = 9.885$ keV at Si(555) backreflection. $L_1 = 1$ m, $l = 100$ mm, $p = 0.3$ mm, (a) $d = 12.6$ mm and (b) $d = 7.54$ mm. The angular deviation from ideal surface $\sigma_{(x,y)} = 20 \mu\text{rad} \times 20 \mu\text{rad}$, source size $\sigma_{ss(x,y)} = 20 \mu\text{m} \times 20 \mu\text{m}$ and intrinsic Darwin width $\Delta E_{\text{int}} = 14.7$ meV (FWHM) are taken into account. (Incident bandwidth is not included.)

Table 5

Calculated contributions to the energy resolution for medium-resolution spectrometers operating at the Si(5 5 5) reflection (short arm length and large solid angle).

$L_1 = 2.0, 1.5$ and 1.0 m and $c = 0.6$ mm, $l = 100$ mm, $p = 0.3$ mm and $D = 100$ mm (corresponding solid angles are $\Omega = 100, 66.7$ and 50 mrad) are selected. We take $d = 10$ mm for cases (I) and (II) and $d = d_{\min} + 2$ mm for cases (III)–(VI). $(\Delta E)_{\text{geom}}$: geometric energy resolution at $E = 9.885$ keV. Results for Si(7 7 7) reflection case at $E = 13.839$ keV are shown in the last row.

	(I)(a)			(II)(a)			(III)			(IV)			(V)			(VI)		
L_1 (m)	2.0	1.5	1.0	2.0	1.5	1.0	2.0	1.5	1.0	2.0	1.5	1.0	2.0	1.5	1.0	2.0	1.5	1.0
L_2 (m)	2.0	1.5	1.0	2.0	1.5	1.0	2.0	1.5	1.0	1.9	1.4	0.9	1.9	1.4	0.9	1.448	0.947	1.448
R (m)	2.0	1.5	1.0	2.0	1.5	1.0	2.0	1.5	1.0	1.949	1.448	0.947	1.949	1.448	0.947	1.949	1.448	0.947
c (mm)	0.6	0.6	0.6	0.6	0.6	0.6	0.6	0.6	0.6	0.6	0.6	0.6	0.6	0.6	0.6	0.6	0.6	0.6
d (mm)	10.0	10.0	10.0	10.0	10.0	10.0	7.60	9.27	12.6	5.09	5.91	7.57	5.09	5.91	7.57	5.09	5.91	7.57
l (mm)	0.0	0.0	0.0	0.0	0.0	0.0	100	100	100	100	100	100	100	100	100	100	100	100
p (mm)	–	–	–	0.3	0.3	0.3	0.3	0.3	0.3	–	–	–	0.3	0.3	0.3	0.3	0.3	0.3
M	1.0	1.0	1.0	1.0	1.0	1.0	1.0	1.0	1.0	0.95	0.93	0.90	0.95	0.93	0.90	0.95	0.93	0.90
δ_0 (mrad)	2.50	3.33	5.00	2.50	3.33	5.00	1.95	3.20	6.63	1.30	2.04	3.98	1.30	2.04	3.98	1.30	2.04	3.98
$\Delta\delta$ (mrad)	0.0	0.0	0.0	0.0	0.0	0.0	1.3	2.4	5.6	1.3	2.4	5.5	1.3	2.4	5.5	1.3	2.4	5.5
ΔT_1 (K)	0.0	0.0	0.0	0.0	0.0	0.0	–0.48	–1.40	–6.70	0.0	0.0	0.0	0.0	0.0	0.0	–0.24	–0.65	–2.74
ΔT_2 (K)	0.0	0.0	0.0	0.0	0.0	0.0	0.48	1.40	6.70	0.0	0.0	0.0	0.0	0.0	0.0	0.41	1.19	5.67
ε_1 (p.p.m.)	0.75	1.33	3.00	–	–	–	–	–	–	–	–	–	–	–	–	–	–	–
ε_2 (p.p.m.)	–	–	–	0.19	0.33	0.75	0.15	0.32	0.99	–	–	–	–	–	–	–	–	–
ε_3 (p.p.m.)	–	–	–	–	–	–	–	–	–	1.72	4.86	22.2	1.72	4.86	22.2	–	–	–
ε_4 (p.p.m.)	–	–	–	–	–	–	–	–	–	–	–	–	–	–	–	0.10	0.21	0.61
ε (p.p.m.)	0.75	1.33	3.00	0.19	0.33	0.75	0.15	0.32	0.99	1.72	4.86	22.2	1.72	4.86	22.2	0.10	0.21	0.61
$(\Delta E)_{\text{geom}}$ (meV)†	7.4	13.2	29.7	1.9	3.3	7.4	1.4	3.2	9.8	17.0	48.0	219	17.0	48.0	219	0.98	2.04	6.01
$(\Delta E)_{\text{sim}}$ (meV)	7.4	13.1	29.6	1.8	3.3	7.2	1.2	3.7	10.7	11.4‡	22.5 (48)‡	57.7‡ (48)‡	5.4, 4.9, 2.9‡	11, 17, 13 (48)‡	53, 78, 40 (57)‡	0.90	1.97	5.2
$(\Delta E)_{\text{geom}}$ (meV)§	11.9	21.1	47.4	3.0	5.3	11.9	2.0	4.4	13.8	23.7	67.0	306.0	23.7	67.0	306.0	2.7	6.6	23.1

† $E = 9.885$ keV. ‡ The differences between the analytic estimation and the simulations are due to asymmetric resolution function from the non-linear energy–position correlations. § $E = 13.839$ keV.

tracing results are shown for quadratic temperature gradient $\Delta E = 23$ meV (FWHM) and a more practical linear gradient $\Delta E = 35$ meV (FWHM). These are much better than without the gradient which has an asymmetric line shape with $\Delta E = 72$ meV (FWHM) or $\Delta E = 232$ meV (full width at tenth of maximum). Similar improvements, though not as dramatic, are also possible in high-resolution configurations.

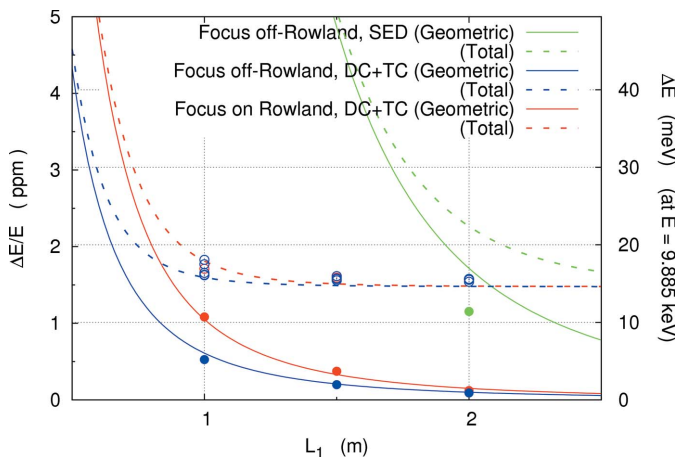


Figure 11 Energy resolution as a function of 2θ arm length, L_1 , for medium-resolution spectrometers. Comparison of a single-element detector (SED) and dispersion compensation (DC) with temperature compensation (TC). Closed and open circles represent simulation results of geometric and total contributions, respectively. Solid lines are geometric terms discussed in Table 5.

7. Some practical considerations

The practical aspects of detector size, momentum-resolution and noise are mentioned in this section. While from the point of view of the dispersion and energy resolution the on-Rowland case is preferable, it leads to a relatively large beam size at the detector, so requires a larger detector and larger d_{\min} . Background in the detector is usually dominated by

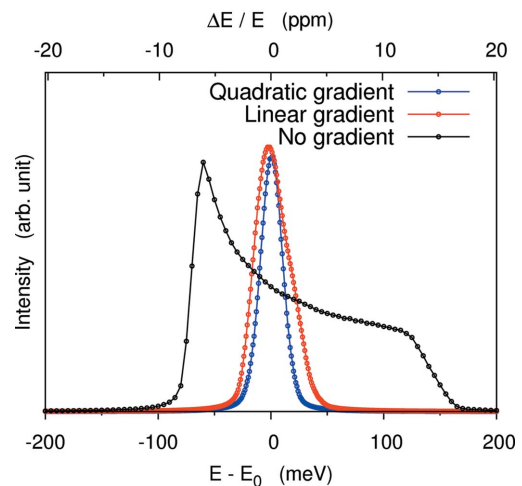


Figure 12 Improved energy resolution using a single-element detector and a temperature gradient in the off-Rowland geometry. Conditions for the simulations are large solid angle, 100 mrad, $E = 9.885$ keV of Si(555) with three different temperature gradients. See text for discussion.

cosmic-ray muon events, and can be expected to scale with area, so the on-Rowland case will have a larger noise, and one should consider count rates in expected experiments carefully. The increased offset, larger d_{\min} , may also become more of an issue as one considers a two-dimensional analyzer array (Baron *et al.*, 2008).

The on-Rowland case, however, offers the possibility to improve momentum resolution using transverse position sensitivity of the detector. The essential idea is that if the detector is not in the horizontal analyzer focus then there is a correlation between horizontal detector position and horizontal analyzer position. In particular, assuming a spherical analyzer the beam size for the on-Rowland case is just Ωl while the blurring owing to the crystallite size (pinhole effect) is just $2c'$. Then, if $\Omega l \gg 2c'$, the detector position sensitivity allows one effective momentum resolution. A correlatory to this is that if one could obtain a single analyzer crystal with very large extent out of the scattering plane, then the position sensitivity might be sufficient such that the single crystal would act as an array. Thus a horizontal analyzer array might be avoided. However, as the limit for analyzer fabrication, at least for high resolution, is really the dicing and bonding process, this would require significant advances in analyzer fabrication technique. It would probably be most interesting for shorter radius arm, where, for example, one might consider a toroidal analyzer, with different radii in the vertical and horizontal, so that the vertical radius might be chosen to match the off-Rowland conditions and so reduce the detector extent, while the horizontal might be chosen to allow the momentum resolution to be determined by the detector.

8. Preliminary temperature gradient experiment

We tested one possibility for creating the required temperature gradient. Fig. 13 shows a schematic of our apparatus. A rectangular piece of silicon is used to simulate the analyzer substrate, and is placed between two copper plates. The silicon analyzer can then be considered as one element in a thermal

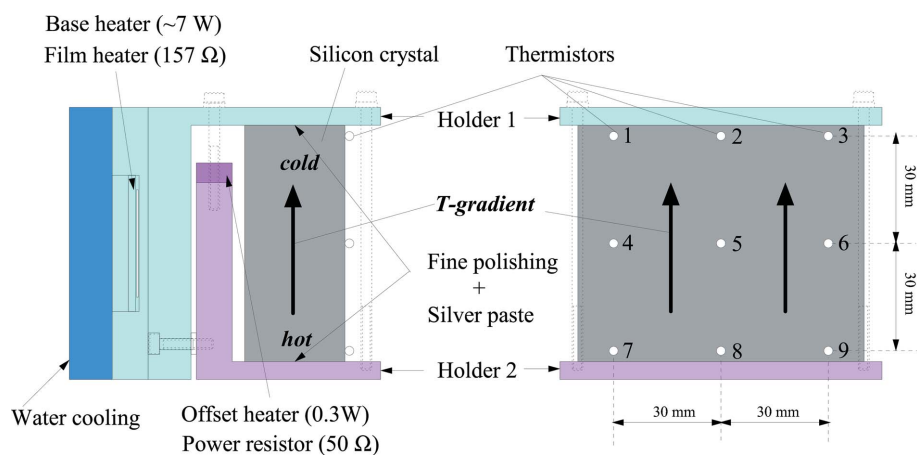


Figure 13 Sketch of a temperature gradient crystal holder. Numbers on the right-hand figure represent the serial numbers of thermistors and are referred to in Table 6. Crystal surface mount thermistors and monitored temperature at each position.

Table 6 Example of a temperature gradient result.

(1) 27.338	(2) 27.341	(3) 27.337
(4) 27.359	(5) 27.359	(6) 27.360
(7) 27.381	(8) 27.379	(9) 27.381

circuit: passing a constant heat flow through the silicon should create the desired gradient. Considering the thermal conductivity of silicon, $1.3 \text{ W cm}^{-1} \text{ K}^{-1}$ at room temperature, and choosing the silicon cross section to be $3 \text{ cm} \times 9 \text{ cm}$ (normal to the flow), one expects that a heat flow of $\sim 0.5 \text{ W}$ will create a temperature difference of 100 mK across 7 cm of silicon.

To test this, we place the holder sketched in Fig. 13 into a vacuum. The base temperature was controlled by a PID system and the offset heater was held at a constant power. The total power to the base heater was about 7 W , while the offset heater was 0.3 W . The temperature distribution over the surface was measured by nine calibrated thermistors that were attached to the surface using silver paste. As one can see from the results in Table 6, the gradient was controllable to within $\pm 3 \text{ mK}$, along a horizontal line. This level of control should allow reduction of a geometrically broadened resolution of 2.2 meV to about 0.6 meV at 22 keV , a reasonable first starting point for this work.

9. Conclusions

The promise of inelastic X-ray scattering has always been offset by the complexity of the necessary spectrometers. However, increased experience, improvements in optics, detectors and overall beamline design make it increasingly possible to consider very sophisticated instrumentation. In contrast, hutch size, and space on the experimental floor remain serious limitations. Thus the suggestion of introducing a temperature gradient on analyzer crystals to reduce spectrometer size for a given resolution, or improve resolution for a fixed size, is both timely and relevant.

Our work suggests $\sim 1.5 \text{ meV}$ energy resolution should be possible at 21.7 keV using a 3 m arm while keeping 200 mm clearance between the sample and the detector, and better than 20 meV resolution at 10 keV with 100 mm clearance. Other points discussed include the possibility to improve the energy resolution even with single-element detectors when the analyzer focus is not on the Rowland circle, and the possibility of using a two-dimensional position-sensitive detector for improving momentum resolution transverse to the analyzer scattering plane without slitting.

References

Baron, A. Q. R., Sutter, J. P., Tsutsui, S., Uchiyama, H., Masui, T., Tajima, S., Heid,

- R. & Bohnen, K. P. (2008). *J. Phys. Chem. Solids*, **69**, 3100–3102.
- Baron, A. Q. R., Tanaka, Y., Goto, S., Takeshita, K., Matsushita, T. & Ishikawa, T. (2000). *J. Phys. Chem. Solids*, **61**, 461–465.
- Burkel, E. (1991). *Inelastic Scattering of X-rays with High Energy Resolution, Springer Tracts in Modern Physics*, Vol. 125. Berlin: Springer.
- Chumakov, A. I., Baron, A. Q. R., Ruffer, R., Grünsteudel, H. F. & Meyer, A. (1996). *Phys. Rev. Lett.* **76**, 4258–4261.
- Dorner, D. & Peisl, J. (1983). *Nucl. Instrum. Methods*, **208**, 587–592.
- Huotari, S., Albergamo, F., Vanko, G., Verbeni, R. & Monaco, G. J. (2006). *Rev. Sci. Instrum.* **77**, 053102.
- Huotari, S., Vankó, Gy., Albergamo, F., Ponchut, C., Graafsma, H., Henriquet, C., Verbeni, R. & Monaco, G. (2005). *J. Synchrotron Rad.* **12**, 467–472.
- Masciovecchio, C., Bergmann, U., Krisch, M., Ruocco, G., Sette, F. & Verbeni, R. (1996a). *Nucl. Instrum. Methods Phys. Res. B*, **111**, 181–186.
- Masciovecchio, C., Bergmann, U., Krisch, M., Ruocco, G., Sette, F. & Verbeni, R. (1996b). *Nucl. Instrum. Methods Phys. Res. B*, **111**, 339–340.
- Miwa, D. (2002). Master's thesis, Himeji Institute of Technology, Japan.
- Mohr, P. J. & Taylor, B. T. (2000). *Rev. Mod. Phys.* **72**, 351–495.
- Okada, Y. & Tokumaru, Y. (1984). *J. Appl. Phys.* **56**, 314–320.
- Seto, M., Yoda, Y., Kikuta, S., Zhang, X. W. & Ando, M. (1995). *Phys. Rev. Lett.* **74**, 3828–3831.
- Sette, F., Kirsch, M. H., Masciovecchio, C., Ruocco, G. & Monaco, G. (1998). *Science*, **280**, 1550–1555.
- Sinn, H., Alp, E. E., Alatas, A., Barazza, J., Bortel, G., Burkel, E., Shu, D., Sturhahn, W., Sutter, J. P., Toellner, T. S. & Zhao, J. (2001). *Nucl. Instrum. Methods Phys. Res. A*, **467–468**, 1545–1548.
- Watanabe, H., Yamada, N. & Okaji, M. (2004). *Int. J. Thermophys.* **25**, 221–236.